#### **RESEARCH PAPER**



# Multiphysics topology optimization of a multifunctional structural battery composite

Reza Pejman<sup>1</sup> · Ahmad Raeisi Najafi<sup>1</sup>

Received: 19 May 2022 / Revised: 11 December 2022 / Accepted: 21 December 2022 © The Author(s), under exclusive licence to Springer-Verlag GmbH Germany, part of Springer Nature 2023

#### **Abstract**

The structural battery composite (SBC) is a novel class of multifunctional materials with the ability to work as a lithium-ion battery that can withstand mechanical loads. The motivation of this study is to address one of the major challenges in the development of SBCs, which is a strong conflict in the structural and electrical demands for its electrolyte (*i.e.*, high stiffness and high ionic conductivity). Furthermore, there is a design requirement that the electrochemical cycling should not result in overheating of the SBC. The novelty of this study is the development of an efficient multi-objective multiphysics density-based topology optimization framework that considers electrochemical/thermal/structural physics to identify the optimized design of a structural battery electrolyte (SBE). The optimization methodology is defined as solving a multi-objective problem of maximizing effective ionic conductivity and minimizing compliance of SBE. The problem is subjected to constraints on volume fraction and the maximum allowable temperature. The normalized-normal-constraint approach is utilized to generate a Pareto-front curve for this multi-objective problem. The proposed method is computationally efficient owing to utilizing a low-fidelity resistance network approach, for the electrochemical module and parallelizes the workload using portable, and extendable toolkit for scientific computing and message-passing interface. Several numerical examples are solved to demonstrate the applicability of the proposed methodology under different loading scenarios. The results reveal that the proposed methodology provides a better understanding of the required microstructural design of SBE for the performance improvement of structural battery composites.

 $\textbf{Keywords} \ \ \text{Topology optimization} \cdot \text{Multiphysics} \cdot \text{Multi-objective} \cdot \text{Multifunctional} \cdot \text{Structural battery composite}$ 

### 1 Introduction

The structural battery composite (SBC) is a new class of multifunctional materials that combines the load-bearing capacity of a carbon fiber composite with the energy-storing capabilities of a lithium-ion battery (Wetzel 2004; Snyder et al. 2007, 2008; Wong et al. 2007; Liu et al. 2009; Ekstedt et al. 2010; Asp and Greenhalgh 2014). The SBC¹ shows promising potential in addressing the issue of "low specific energy" in lithium-ion batteries (Johannisson et al. 2019; Carlstedt and Asp 2020). In these materials, carbon fiber works both as a high-performance structural reinforcement

Responsible Editor: Seonho Cho

Published online: 18 February 2023

Ahmad Raeisi Najafi arn55@drexel.edu

and a lithium-ion battery electrode. The composite polymeric matrix (typically referred to as structural battery electrolyte (SBE)) is also in charge of two tasks: (1) transferring the structural load and (2) working as a lithium-ion battery electrolyte.

Similar to most multifunctional materials, the physical property demands for multifunctionality in SBE (*i.e.*, high stiffness and high ionic conductivity) are intrinsically conflicting as shown in Fig. 1 (Asp 2013). In the figure, the shaded area indicates desired properties of the SBE for a high-performance structural battery. Any modification of the constituents to enhance one function results in a substantial reduction in the other function. For this reason, the design of SBE for high-performance structural batteries is mentioned as one of the most challenging aspects of this research field (Asp and Greenhalgh 2015). Moreover, as indicated by Shirshova et al. (2013), the key to alleviating such a conflict

<sup>&</sup>lt;sup>1</sup> Structural battery composite is also referred to as "massless battery".



Department of Mechanical Engineering and Mechanics, Drexel University, Philadelphia, PA 19104, USA

46 Page 2 of 17 R. Pejman, A. R. Najafi

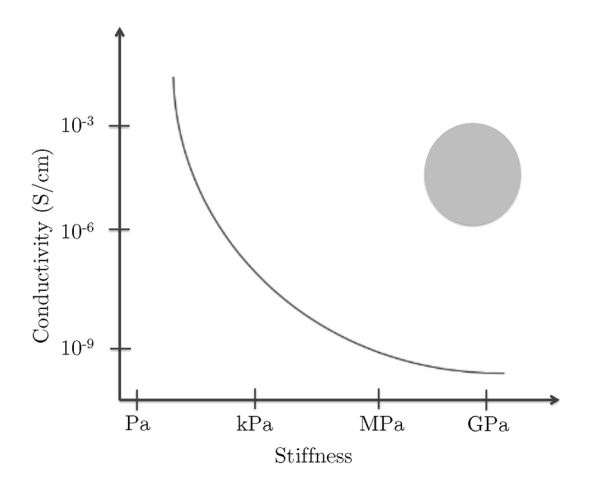


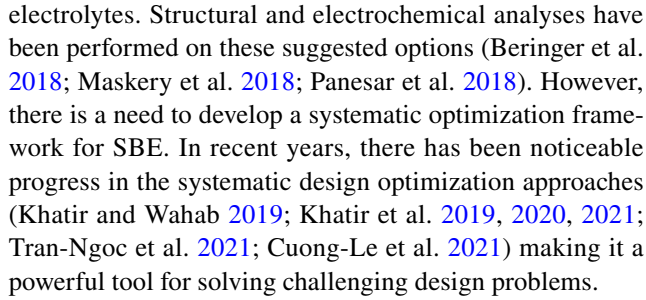
Fig. 1 Schematic of the ion conductivity vs. stiffness for structural battery electrolyte. The shaded area indicates desired properties of the SBE for a high-performance structural battery. Reproduced figure from Asp (2013) by permission of Taylor & Francis Ltd (copyright © Institute of Materials, Minerals, and Mining, reprinted by permission of Taylor & Francis Ltd, http://www.tandfonline.com on behalf of Institute of Materials, Minerals, and Mining.)

is through better control of SBE microstructures. Thus, there is an absolute need for a systematic design framework for the microstructural design of SBE.

One of the major concerns in the development of polymeric SBE is related to the high amount of heat generation. The ionic conductivity of solid polymer electrolytes used in structural batteries is several orders of magnitudes smaller than the ionic conductivity in ordinary liquid electrolytes used in lithium-ion batteries (Xu 2004; Willgert et al. 2011; Ihrner et al. 2017). As a result, the ohmic heat generation rate will be substantially higher in the structural batteries in comparison with lithium-ion batteries (Carlstedt and Asp 2019; Pejman et al. 2021; Pejman et al. 2022). It is essential to consider this matter while designing the SBEs microstructure. Thus, we are dealing with a multiphysics problem that includes structural, electrochemical, and thermal physics.

In general, polymeric electrolytes are composed of two phases: (1) solid phase for providing structural integrity and (2) compliant phase for enhancing ionic conductivity. The solid phase has high stiffness and thermal conductivity and low ionic conductivity, while the compliant phase has low stiffness and thermal conductivity, and high ionic conductivity. The goal is to determine the ideal microstructures for these two phases to address the aforementioned conflicting physical demands.

Several studies in the literature proposed potential microstructures for structural electrolytes (Beringer et al. 2018; Maskery et al. 2018; Panesar et al. 2018). For instance, truss-like lattice structures, body-centered cubic lattices, and Schwarz's primitive minimal surface have been proposed as interesting potential microstructures for structural



To the best of our knowledge, there is only one study that presents a rigorous design optimization framework for SBE. In this study, Lee et al. proposed a multi-objective topology optimization approach to optimize the microstructure of SBE (Lee et al. 2019). They used the weighted average multi-objective scheme to simultaneously maximize electrical power and minimize compliance for a unit cell. However, in their study, they have not considered the thermal physics as well as the effect of the presence of carbon fibers on the optimized microstructure of SBE. As it is highlighted in Asp and Greenhalgh (2015), introducing reinforcement fibers is expected to result in a different matrix microstructure from that in the bulk condition.

In this study, we present a multiphysics, multi-objective gradient-based topology optimization framework to maximize the ionic conductivity and stiffness of SBE. We consider constraints on the maximum allowable temperature as well as void volume fraction. The topology optimization approach has shown a profound ability for material designs in structural (Larsen et al. 1997; Bruns and Tortorelli 2001; Rozvany 2001; Guest 2009; Le et al. 2010; Holmberg et al. 2014), thermal (Borrvall and Petersson 2003; Gersborg-Hansen et al. 2006; Matsumori et al. 2013; Zhao et al. 2018; Pejman et al. 2021), electrochemical (Yaji et al. 2018; Onishi et al. 2019), and also multiphysics problems (Guest and Prévost 2006; Dede 2009; Zhu et al. 2019; Kambampati et al. 2021). Our method of choice for the multi-objective scheme is the normalized-normal-constraint (NNC) approach which shows superior performance over the weighted-average scheme as reported in Messac et al. (2003).

One of the difficulties in solving multiphysics optimization problems is the typical high computational costs associated with solving several physics in each iteration of the optimization process. To alleviate this issue, we implement a low-fidelity resistance network (ResNet) approach for the electrochemical module (Rhazaoui et al. 2013; Rhazaoui et al. 2014). This method has been previously validated via an experiment in Rhazaoui et al. (2015). There are also high-fidelity models available in the literature for evaluating ionic conductivity (Mu et al. 2007; Choi et al. 2011), however, they often deal with the complex electrochemical mechanisms of ion migration which come at a high computational cost. Moreover, due to the complexity of the multiphysics optimization problem, the only feasible way to obtain a



solution with a reasonable computational cost is to use parallel computations. To this end, we developed our code in C++ language utilizing the portable and extendable toolkit for scientific computing (PETSc) (Balay et al. 2021), and the parallelization is performed with aid of the Message-Passing Interface (MPI) that allows for distributing the computational memory and workload over several processors. It has been shown previously that performing topology optimization using C++ and PETSc reduces the computational cost extensively (Aage et al. 2015; Kambampati et al. 2020).

The main contribution of this study is as follows: (1) to the best of our knowledge, there is not any study in the literature to present a systematic multi-objective topology optimization framework for the design of SBE microstructure by simultaneously considering electrochemical, structural, and thermal physics, and (2) this study is the first to attempt addressing the issue of designing SBE microstructure by considering carbon fibers in the design space as mentioned in Asp and Greenhalgh (2015).

The remainder of the paper is organized as follows: Sect. 2 presents the multiphysics model and finite element discretization. We introduce the multiphysics topology optimization scheme and perform the sensitivity analysis in Sect. 3. A few numerical optimization examples are solved in Sect. 4 including the design of matrix microstructure for the bulk condition and also for the situation that we incorporate reinforcement fibers in the design space. Finally, Sect. 5 summarizes the contribution of this research, limitations of the proposed approach, and suggestions for future studies.

## 2 Multiphysics model

The problem setup is shown in Fig. 2. A laminated structural battery is considered. In the negative and positive electrodes, carbon fibers are embedded in a porous matrix (*i.e.*, SBE). The separator<sup>2</sup> is assumed to be made from SBE. The domain  $\Omega$  consists of SBE material that is represented by domain  $\Omega_{SBE}$  and the carbon fibers that are indicated by  $\Omega_{cf}$ . The boundary of the domain  $\Omega$  is divided into four complementary subsets:  $\Gamma_V$ ,  $\Gamma_U$ ,  $\Gamma_F$ , and  $\Gamma_h$ . Voltage  $v^p$ , displacement  $u^p$ , and structural load  $s^p$  are prescribed over  $\Gamma_V$ ,  $\Gamma_U$ , and  $\Gamma_F$ , respectively. And convection heat transfer with the ambient environment is considered over  $\Gamma_h$ .

The multiphysics model considered in this study includes electrochemical, structural, and thermal physics. In the electrochemical module, we aim to compute the effective ionic conductivity of the SBE. To do so, we use the ResNet approach suggested in Rhazaoui et al. (2013), (2014). For

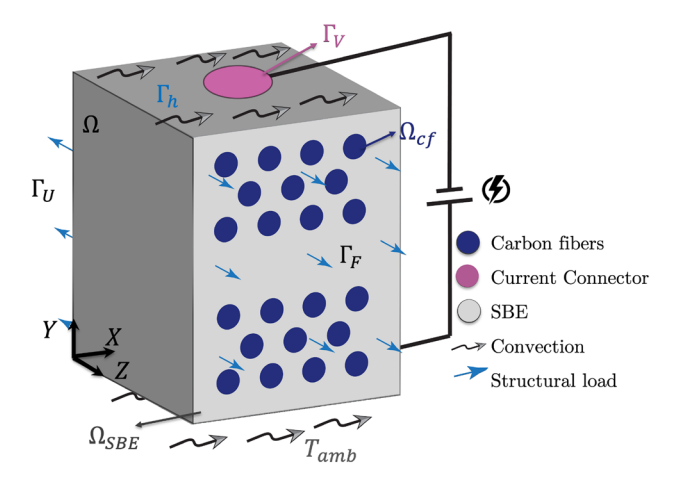


**Fig. 2** Schematic of the problem setup for multiphysics model of SBE. Note that  $\Gamma_U$  is applied on the plane parallel to XY-plane with  $Z = Z_{max}/2$ ,  $\Gamma_h$  is applied to the top and beneath surfaces, and  $\Gamma_F$  is applied to the front and back surfaces

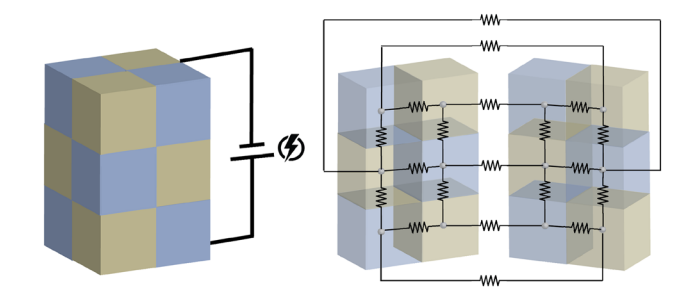


Fig. 3 Equivalent resistor network of a  $2 \times 2 \times 3$  voxel structure, with the nodes positioned at the center of each voxel

completeness, we summarize the governing equations associated with the ResNet model in Sect. 2.1. In the structural module, the goal is to find the compliance of the SBE by solving a linear elasticity problem. The governing equations related to structural physics are presented in Sect. 2.2. And finally, we solve the convection-diffusion thermal energy equation to find the temperature distribution in the SBE. Note that the thermal module is weakly-coupled to the electrochemical module since the amount of generated heat in the SBE is computed using the ohmic heat generation equation. The governing equations associated with the thermal module are summarized in Sect. 2.3.

### 2.1 Electrochemical module

In this model, the 3D microstructure needs to be discretized into voxels (*i.e.*, small cubic elements), and then, a resistor network is drawn for the voxelized structure as shown in Fig. 3. By applying a potential difference to the network, the corresponding currents are computed, allowing for



<sup>&</sup>lt;sup>2</sup> The existence of a separator lamina assures that the active electrode materials in the two electrodes do not come in contact.

calculating the equivalent resistance and consequently, the ionic conductivity of the entire structure. Note that in this study, we consider each finite element as a voxel.

The resistance of voxel k can be defined as

$$R_k = \frac{l_{vox}}{\sigma_k A_{vox}} \tag{1}$$

where  $\sigma_k$  is the conductivity of the material in voxel k. The length of a voxel along the direction of current flow is shown by  $l_{vox}$  and the cross-sectional area of a voxel perpendicular to current flow is indicated by  $A_{vox}$ .

The resistance between two face-sharing voxels is given by

$$R_{ij} = \alpha_i R_i + \alpha_j R_j, \quad \alpha = \begin{cases} 1/2 \text{ For internal elements} \\ 1 \text{ For boundary elements} \end{cases}$$
 (2)

where  $R_i$  and  $R_j$  denote the resistances of the *i*th and *j*th elements, respectively. And  $R_{ij}$  shows the equivalent resistance between the two voxels that share a common face.

By writing Kirchhoff's law of current conservation, a system of linear equations ( $\mathbb{ZV} = \mathbb{I}$ ) will be obtained, where  $\mathbb{Z}$  is the global ionic conductivity matrix,  $\mathbb{V}$  is the global potential vector, and  $\mathbb{I}$  is the global current vector.

The components of the global ionic conductivity matrix are defined as:

$$Z_{ii} = -\sum_{j \in N_c} \frac{1}{R_{ij}} \tag{3}$$

$$Z_{ij} = \begin{cases} \frac{1}{R_{ij}} & j \in N_i \\ 0 & j \notin N_i, i \neq j \end{cases}$$
 (4)

where  $Z_{ii}$  and  $Z_{ij}$  denote the diagonal and non-diagonal components of the global ionic conductivity matrix, respectively.  $N_i$  is a set of voxels that share a face with the *i*th voxel.

In terms of the boundary conditions, we assume that the potential at the inlet  $(V_{in})$  and outlet  $(V_{out})$  voxels (i.e.), the locations where current connectors are introduced) are known. In order to compute the potential vector, we need to solve the following equation:

$$\mathbb{Z}^* \mathbb{V} = \mathbb{V}^* \tag{5}$$

where all the components of  $\mathbb{V}^*$  are zero except the ones that are coincident with the current connectors and they have either  $V_{in}$  or  $V_{out}$  values. Note that  $\mathbb{Z}^*$  is the ionic conductivity matrix after applying the boundary condition.

Having the potential vector allows for solving the system of linear equations  $\mathbb{Z}\mathbb{V}=\mathbb{I}$  to find the current vector. The inlet and outlet current values can be computed by



where  $N_{in}$  and  $N_{out}$  are the set of boundary voxels at the inlet and outlet, respectively. Potential difference is given by  $\Delta V = V_{out} - V_{in}$ . Note that  $I_{in} = -I_{out}$ . The equivalent resistance can be computed as  $R_{eq} = \frac{\Delta V}{I_{out}}$ . And finally, the effective ionic conductivity is defined as follows:

$$\mathcal{K}_{eff} = \frac{I_{out}t_{ec}}{\Delta V A_{cc}} \tag{7}$$

where  $t_{ec}$  is the thickness of SBC, parallel to the current flow, and  $A_{ec}$  is the surface area perpendicular to the current flow. Note that we assume the current flow is in the +Y direction as shown in Fig. 2. The accuracy of the ResNet model obtained in this study is checked and confirmed against the test cases provided in Rhazaoui et al. (2013).

#### 2.2 Structural module

Three-dimensional linear static formulation under the assumption of small deformation is considered. The computational domain is discretized by 8-node hexahedron finite elements. Implementation of the finite element method (FEM) leads to the following system of linear equations:

$$\mathbb{K}_{S}\mathbb{U} = \mathbb{F}_{S} \tag{8}$$

where  $\mathbb{K}_S$  is the global stiffness matrix,  $\mathbb{U}$  is the global nodal displacement vector, and  $\mathbb{F}_S$  represents the global nodal force vector.

Using isoparametric formulation, the elemental stiffness matrix  $\mathbf{K}_{S}^{e}$  and the elemental force vector  $\mathbf{F}_{S}^{e}$  are given by

$$\mathbf{K}_{S}^{e} = \int_{\Omega^{e}} \mathbf{B}_{S}^{e'} \mathbb{C} \mathbf{B}_{S}^{e} d\Omega \tag{9}$$

and

$$\mathbf{F}_{S}^{e} = \int_{\hat{\Omega}} \mathbf{N}_{S}^{e'} \mathbf{b} d\Omega + \int_{\Gamma_{F}} \mathbf{N}_{S}^{e'} \mathbf{s}^{\mathbf{p}} d\Gamma$$
 (10)

respectively.  $S^{\mathbf{P}}$  is the linearized Piola–Kirchoff stress tensor and  $\mathbf{b}$  is the body force. Further details regarding defining the terms used in Eqs. (9) and (10) are provided in Appendix A.  $\mathbb{C}$  is the elasticity tensor for isotropic materials defined in Eqs. (A5).  $\mathbf{N}_S^e$  and  $\mathbf{B}_S^e$  are introduced in Eqs. (A2) and (A4), respectively. Note that in this study, we do not consider body force; hence the first term in Eq. (10) is zero (see Fig. 2). As usual,  $\mathbb{K}_S$  and  $\mathbb{F}_S^e$  are assembled from  $\mathbf{K}_S^e$  and  $\mathbf{F}_S^e$ , respectively. The compliance is then computed by



$$c = \mathbb{F}_{S}^{'} \mathbb{U} \tag{11}$$

We verify the structural module against ANSYS in "Appendix C".

#### 2.3 Thermal module

The thermal module deals with solving the energy equation in a steady-state condition. Note that in terms of the boundary condition, we assume convection heat transfer boundary condition on  $\Gamma_h$  and insulated boundary condition on all other boundaries (see Fig. 2).

Per usual, implementing FEM results in the following system of linear equations:

$$\mathbb{K}_T \mathbb{T} = \mathbb{F}_T \tag{12}$$

where  $\mathbb{K}_T$  is the global stiffness matrix,  $\mathbb{T}$  is the global nodal temperature vector, and  $\mathbb{F}_T$  is the global nodal force vector.

The elemental stiffness matrix  $\mathbf{K}_T^e$  and the elemental force vector  $\mathbf{F}_T^e$  are given by

$$\mathbf{K}_{T}^{e} = \int_{\Omega} \mathbf{B}_{T}^{e'} \mathbf{k} \mathbf{B}_{T}^{e'} d\Omega + \int_{\Gamma_{h}} h \mathbf{N}_{T}^{e'} \mathbf{N}_{T}^{e} d\Gamma$$
(13)

and

$$\mathbf{F}_{T}^{e} = \int_{\Omega} \mathbf{N}_{T}^{e'} \ Q_{gen} d\Omega + \int_{\Gamma_{h}} h \mathbf{N}_{T}^{e'} \ T_{amb} d\Gamma, \tag{14}$$

respectively. **k** is the thermal conductivity tensor, h is the convection coefficient,  $Q_{\text{gen}}$  is the heat generation rate, and  $T_{\text{amb}}$  is the ambient temperature. More details regarding defining the terms used in Eqs. (13) and (14) are provided in Appendix B.  $\mathbf{N}_T^e$  and  $\mathbf{B}_T^e$  are introduced in Eqs. (B7) and (B9), respectively.

Having the elemental stiffness matrix and force vector allows for assembling  $\mathbb{K}_T$  and  $\mathbb{F}_T$ , respectively. The accuracy of the thermal module is verified against FLUENT in Appendix C. It is worth mentioning that in this study, the same domain discretization is used for all analysis modules (*i.e.*, electrochemical, structural, and thermal).

# 3 Multiphysics topology optimization scheme

In this study, we aim to solve a multi-objective design optimization problem to find the ideal microstructure for SBE. The competing objectives are to minimize compliance (cf. Eq. (11)) and maximize the effective ionic conductivity (cf. Eq. (7)) of the SBE (*i.e.*,  $\theta(\mathbb{U}(\mathbf{X}, \boldsymbol{d}), \mathbb{I}(\mathbf{X}, \boldsymbol{d}), \mathbf{X}, \boldsymbol{d})$ , where  $\boldsymbol{d}$  is the vector of design parameters). The design problem is considered to be subjected to a set of constraints such

as maximum allowable temperature and volume fraction. Note that instead of maximizing the ionic conductivity of the SBE, we can minimize the negative of ionic conductivity. Let's denote the vector of objective functions as  $\boldsymbol{\theta} = \{\theta_1, \theta_2\}$ , where  $\theta_1$  indicates the negative of ionic conductivity and  $\theta_2$  denotes compliance. The multiphysics, multi-objective optimization problem can be formulated as

$$\min_{\boldsymbol{d}} \boldsymbol{\theta}(\mathbb{U}(\mathbf{X}, \boldsymbol{d}), \mathbb{I}(\mathbf{X}, \boldsymbol{d}), \mathbf{X}, \boldsymbol{d}),$$
 such that :  $0 \le d_i \le 1$ ,  $\mathbf{g}(\mathbb{T}(\mathbb{I}(\mathbf{X}, \boldsymbol{d}), \mathbf{X}, \boldsymbol{d}), \mathbf{X}, \boldsymbol{d}) \le \mathbf{0}$ ,  $\mathbf{h}(\mathbf{X}, \boldsymbol{d}) = \mathbf{0}$ , (15) and  $\mathbb{Z}\mathbb{V} = \mathbb{I}$ ,  $\mathbb{K}_S\mathbb{U} = \mathbb{F}_S$ ,  $\mathbb{K}_T\mathbb{T} = \mathbb{F}_T$ 

where  ${\bf g}$  is the inequality constraint associated with the maximum allowable temperature, and  ${\bf h}$  is the equality constraint representing the volume fraction of the solid component. Note that since maximizing ionic conductivity means having a more compliant phase and maximizing stiffness means having a more solid phase, an equality constraint on the volume fraction is imposed for this multi-objective design problem. However, in general, this is not a limitation of the proposed design approach in this study. It is also possible to use a range for the volume fraction with the proposed method.

Let  $\mathscr{S}$  denote the set of feasible solutions to the multiobjective optimization problem Eq. (15). To generate the Pareto front, we use the normalized normal constraint (NNC) method introduced in Messac et al. (2003). The central idea in this method is to sequentially restrict  $\mathscr{S}$  to generate the solutions along the Pareto optimal front as schematically shown in Fig. 4. The process of generating the Pareto optimal front can be summarized in the following steps:

Step 1: Finding the anchor points shown by the blue circles in Fig. 4a by performing single-objective optimizations on  $\theta_1$  and  $\theta_2$  to obtain  $\theta_1(d_1^*)$  and  $\theta_2(d_2^*)$ . Note that the optimized solution of single-objective optimizations with  $\theta_1$  is denoted by  $d_1^*$  and the optimized solution of single-objective optimizations with  $\theta_2$  is represented by  $d_2^*$ . And then evaluate the value of other objective function at  $d_1^*$  and  $d_2^*$ , i.e.,  $\theta_1(d_2^*)$  and  $\theta_2(d_1^*)$ . In the case of using a range for solid-phase volume fraction constraint, it is expected that the optimizer uses the lower-bound value of that range for finding the anchor point that maximizes the ionic conductivity and the upperbound value for obtaining the anchor point that minimizes the compliance.

Step 2: Mapping the design metric space to the normalized coordinate system ( $\bar{\theta}_1\bar{\theta}_2$ )-plane as shown in Fig. 4b. To do so, we need to define the normalized objective functions as



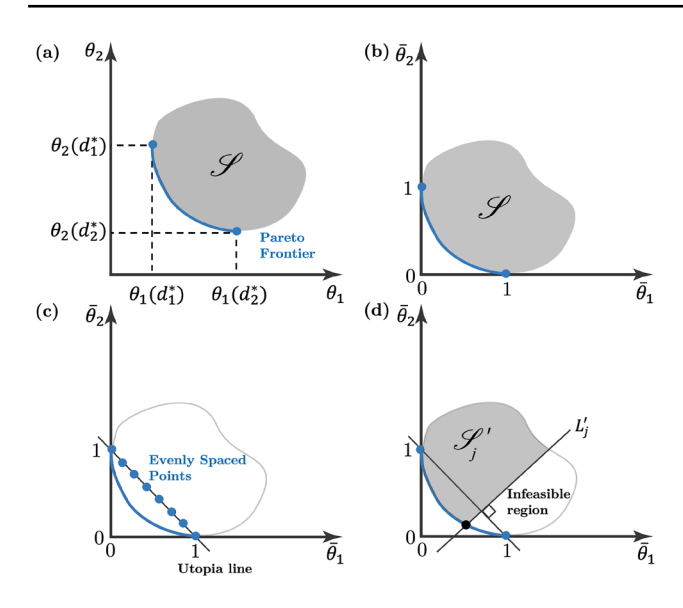


**Fig. 4** Normalized normal constraint (NNC) method: **a** schematic of the feasible region and Pareto Frontier and obtaining the anchor points (blue circles), **b** transformation to the normalized coordinate system, **c** set of evenly spaced points on the Utopia line, and **d** minimization of  $\bar{\theta}_2$  in the new feasible region  $\mathscr{S}_j$  to obtain the black circle on the Pareto Frontier

$$\bar{\theta}_{1}(\mathbf{d}) = \frac{\theta_{1}(\mathbf{d}) - \theta_{1}(\mathbf{d}_{1}^{*})}{\theta_{1}(\mathbf{d}_{2}^{*}) - \theta_{1}(\mathbf{d}_{1}^{*})}, 
\bar{\theta}_{2}(\mathbf{d}) = \frac{\theta_{2}(\mathbf{d}) - \theta_{2}(\mathbf{d}_{2}^{*})}{\theta_{2}(\mathbf{d}_{1}^{*}) - \theta_{2}(\mathbf{d}_{2}^{*})}$$
(16)

where  $\bar{\theta}_1(\mathbf{d_1^*}) = 0$ ,  $\bar{\theta}_1(\mathbf{d_2^*}) = 1$ ,  $\bar{\theta}_2(\mathbf{d_1^*}) = 1$ , and  $\bar{\theta}_2(\mathbf{d_2^*}) = 0$ .

Step 3: Selecting N evenly spaced points on the Utopia line as shown in Fig. 4c. We can write the Utopia line's equation as  $\bar{\theta}_2 = 1 - \bar{\theta}_1$  and the coordinate of each point selected on the Utopia line in the  $(\bar{\theta}_1\bar{\theta}_2)$ -plane as  $(\frac{N-j}{N-1},\frac{j-1}{N-1})$ , where j=2,...,N-1.

Step 4: In this final step, we solve the following optimization problem to obtain the *j*th Pareto point:

$$\begin{aligned} \min_{\boldsymbol{d}} \bar{\theta}_2(\mathbb{U}(\mathbf{X},\boldsymbol{d}),\mathbf{X},\boldsymbol{d}), \\ \text{such that} : & 0 \leq d_i \leq 1, \\ & \mathbf{g}((\mathbb{T}(\mathbb{X},\boldsymbol{d}),\mathbf{X},\boldsymbol{d}),\mathbf{X},\boldsymbol{d})) \leq \mathbf{0}, \\ & \mathbf{h}(\mathbf{X},\boldsymbol{d}) = \mathbf{0}, \\ & \bar{\theta}_1(\mathbb{I}(\mathbf{X},\boldsymbol{d}),\mathbf{X},\boldsymbol{d}) - \bar{\theta}_2(\mathbb{U}(\mathbf{X},\boldsymbol{d}),\mathbf{X},\boldsymbol{d}) \\ & - \frac{j-1}{N-1} + \frac{N-j}{N-1} \leq 0, \\ \text{and} & \mathbb{Z}\mathbb{V} = \mathbb{I}, \\ & \mathbb{K}_S\mathbb{U} = \mathbb{F}_S, \end{aligned} \tag{17}$$

 $\mathbb{K}_T \mathbb{T} = \mathbb{F}_T$ 

where the third constraint enforces the solution to be in  $s'_j$  as shown in Fig. 4d. Note that the optimization problem Eq. (17) needs to be solved for each j, (i.e., a total of N-2 times), to generate the required points on the Pareto optimal front curve. In this study,  $\bar{\theta}_1$  and  $\bar{\theta}_2$  are assumed to be normalized ionic conductivity and normalized compliance, respectively.

Density-based topology optimization is selected to perform the optimization process. Let us discretize the domain with m equi-size hexahedron elements. We associated the density ( $\rho$ ) of zero to the compliant phase of the SBE, and the density of one to the solid phase. The vector of elemental densities can be represented by  $\rho = \{\rho_e\} \in [0,1]$ , for e = 1,2,...,m. In general,  $\rho$  can be partitioned into active elements (design variables)  $\rho_a$  and passive elements  $\rho_p$ . Passive elements are indeed parts of the structure where the density is pre-defined and they are not part of the design space for optimization.

Using the relaxed Heaviside projection proposed in Guest et al. (2004); Wang et al. (2011), the set of physical variables  $\hat{\rho}$  can be defined as

$$\hat{\rho}_e = \frac{\tanh(\beta\eta) + \tanh(\beta(\tilde{\rho}_e - \eta))}{\tanh(\beta\eta) + \tanh(\beta(1 - \eta))}$$
(18)

where  $\eta$  and  $\beta$  are threshold and sharpness factors, respectively.  $\tilde{\rho} = H\rho$  is the filtered field (Bruns and Tortorelli 2001), and **H** is a linear operator given by

$$\mathbf{H}(\rho_e, r_{min}) = \frac{\sum_{i \in N_e} h_{e,i} \rho_i}{\sum_{i \in N_e} h_{e,i}}$$
(19)

where  $N_e = \{i \mid dist(elem_i, elem_e) \leq r_{min} \}$ ,  $h_{e,i} = max(0, r_{min} - dist(elem_i, elem_e))$ , and  $dist(elem_i, elem_e)$  denotes the Euclidean distance between the centroids of element e and i.

The projected density  $(\hat{\rho}_e)$  can be incorporated in the Solid Isotropic Material with Penalization (SIMP) interpolation equation to relate the modulus of elasticity, ionic conductivity, and thermal conductivity of SBE to projected densities as shown in Eq. (20).

$$E_{e}(\hat{\rho}_{e}) = E_{min} + \hat{\rho}_{e}^{\mathfrak{p}}(E_{max} - E_{min}),$$

$$\sigma_{e}(\hat{\rho}_{e}) = \sigma_{max} + \hat{\rho}_{e}^{\mathfrak{p}}(\sigma_{min} - \sigma_{max}),$$

$$k_{e}(\hat{\rho}_{e}) = k_{min} + \hat{\rho}_{e}^{\mathfrak{p}}(k_{max} - k_{min})$$
(20)

where  $E_e$ ,  $\sigma_e$ , and  $k_e$  are the modulus of elasticity, ionic conductivity, and thermal conductivity of element e.  $E_{min}$ ,  $\sigma_{max}$ , and  $k_{min}$  are the modulus of elasticity, ionic conductivity, and thermal conductivity of the compliant phase, and  $E_{max}$ ,  $\sigma_{min}$ , and  $k_{max}$  are the modulus of elasticity, ionic conductivity, and thermal conductivity of the solid phase.  $\mathfrak{p}$  is the penalization power.



# 3.1 Sensitivity analysis

Since the optimization method used in this study is gradient-based, we need to perform a sensitivity analysis of the objective and constraints function with respect to the design variables.

The objective function in the structural module is compliance which can be defined as

$$c(\hat{\boldsymbol{\rho}}) = \mathbb{F}_{S}^{'} \mathbb{U}(\hat{\boldsymbol{\rho}}) \tag{21}$$

where  $(\cdot)'$  denotes transpose. The derivative of compliance with respect to the projected density is given by

$$\frac{\partial c}{\partial \hat{\rho}_e} = -\mathbb{U}' \frac{\partial \mathbb{K}_S}{\partial \hat{\rho}_e} \mathbb{U} \tag{22}$$

where  $\frac{\partial \mathbb{K}_S}{\partial \hat{\rho}_e}$  can analytically be computed using the following equations:

$$\frac{\partial \mathbf{K}_{S}^{e}}{\partial \hat{\rho}_{e}} = \int_{\Omega} \mathbf{B}_{S}^{e'} \frac{\partial \mathbb{C}}{\partial \hat{\rho}_{e}} \mathbf{B}_{S}^{e'} d\Omega \tag{23}$$

and

$$\frac{\partial C}{\partial \hat{\rho}_{e}} = 2 \frac{\partial \mu}{\partial \hat{\rho}_{e}} \mathbb{P}_{Sym} + \frac{\partial \lambda}{\partial \hat{\rho}_{e}} \mathbf{I} \otimes \mathbf{I}$$
(24)

The sensitivity of compliance with respect to the design variables  $(\rho_e)$  is recovered by

$$\frac{\partial c}{\partial \boldsymbol{\rho}} = \frac{\partial \hat{\boldsymbol{\rho}}}{\partial \tilde{\boldsymbol{\rho}}} \odot (\mathbf{H}' \frac{\partial c}{\partial \hat{\boldsymbol{\rho}}}) \tag{25}$$

where

$$\frac{\partial \hat{\boldsymbol{\rho}}}{\partial \hat{\boldsymbol{\rho}}} = \beta \frac{1 - \tanh(\beta(\hat{\boldsymbol{\rho}} - \eta))^2}{\tanh(\beta \eta) + \tanh(\beta(1 - \eta))}$$
 (26)

Effective ionic conductivity computed in the electrochemical module is considered as one of the objective functions. We can re-write Eq. (7) as

$$\mathcal{K}_{eff} = C \sum_{i \in N_{out}} \mathbb{Z}(i, :) \mathbb{V}$$

$$= C \overline{\mathbb{Z}}' \mathbb{V}$$
(27)

where  $C = \frac{t_{ec}}{\Delta V A_{ac}}$  is a constant, and  $\bar{\mathbb{Z}} = \sum_{i \in N_{out}} \mathbb{Z}(i, :)$ .

To perform the sensitivity analysis, we need to take the derivative of Eq. (27) with respect to the projected density as follows:

$$\frac{d\mathcal{K}_{eff}}{d\hat{\rho}_{i}} = \left(\frac{\partial \mathcal{K}_{eff}}{\partial \bar{z}}\right)' \frac{\partial \bar{z}}{\partial \hat{\rho}_{i}} + \left(\frac{\partial \mathcal{K}_{eff}}{\partial \mathbb{V}}\right)' \frac{\partial \mathbb{V}}{\partial \hat{\rho}_{i}} + \frac{\partial \mathcal{K}_{eff}}{\partial \hat{\rho}_{i}}$$
(28)

Note that  $\frac{\partial \mathscr{K}_{eff}}{\partial \hat{\rho}_i}$  is zero since  $\mathscr{K}_{eff}$  is not explicitly function of  $\hat{\rho}_i$ . We can simplify Eq. (28) as

$$\frac{d\mathcal{K}_{eff}}{d\hat{\rho}_{i}} = C\left(\mathbb{V}'\frac{\partial\bar{\mathbb{Z}}}{\partial\hat{\rho}_{i}} + \bar{\mathbb{Z}}'\frac{\partial\mathbb{V}}{\partial\hat{\rho}_{i}}\right). \tag{29}$$

The only unknown on the right-hand side of Eq. (29) is  $\frac{\partial \mathbb{V}}{\partial \hat{\rho}_i}$ . We can use the adjoint sensitivity analysis approach to perform the sensitivity analysis. The central idea in the adjoint sensitivity analysis is to annihilate  $\partial \mathbb{V}/\partial \hat{\rho}_i$  from Eq. (29) instead of directly computing it. To do so, we first rearrange the terms in the pseudo-problems (

$$\mathbb{Z}^* \partial \mathbb{V} / \partial \hat{\rho}_i = -\partial \mathbb{Z}^* / \partial \hat{\rho}_i \mathbb{V} = \mathbb{E}_{pseudo}^i$$

) and then add those terms to Eq. (29). Note that the pseudoproblems are obtained by differentiating the primal problem Eq. (5) with respect to  $\hat{\rho}_i$ .

$$\frac{d\mathcal{K}_{eff}}{d\hat{\rho}_{i}} = C\left(\mathbb{V}'\frac{\partial\overline{\mathbb{Z}}}{\partial\hat{\rho}_{i}} + \overline{\mathbb{Z}}'\frac{\partial\mathbb{V}}{\partial\hat{\rho}_{i}}\right) + \lambda'_{E}\left(\mathbb{Z}^{*}\frac{\partial\mathbb{V}}{\partial\hat{\rho}_{i}} + \frac{\partial\mathbb{Z}^{*}}{\partial\hat{\rho}_{i}}\mathbb{V}\right)$$
(30)

where  $\lambda_E$  is the arbitrary adjoint variable, and

$$_{E}\mathbb{F}_{pseudo}^{i}=-rac{\partial\mathbb{Z}^{*}}{\partial\hat{
ho}_{i}}\mathbb{V}$$

. Note that the last term that we added to Eq. (30) is actually zero. We then rearrange the terms in Eq. (30) to isolate  $\frac{\partial \mathbb{V}}{\partial \hat{a}}$ .

$$\frac{d\mathcal{K}_{eff}}{d\hat{\rho}_{i}} = C\left(\mathbb{V}'\frac{\partial\overline{\mathbb{Z}}}{\partial\hat{\rho}_{i}}\right) + \lambda'_{E}\left(\frac{\partial\mathbb{Z}^{*}}{\partial\hat{\rho}_{i}}\mathbb{V}\right) + \left(C\overline{\mathbb{Z}}' + \lambda'_{E}\mathbb{Z}^{*}\right)\frac{\partial\mathbb{V}}{\partial\hat{\rho}_{i}}$$
(31)

We need to select the arbitrary adjoint variable  $\lambda_E$  in such a way that it makes the coefficient of  $\frac{\partial V}{\partial \hat{\rho}_E}$  zero:

$$\mathbb{Z}^{*'}_{E} = -C\overline{\mathbb{Z}} = -\sum_{i \in N_{\text{out}}} C\mathbb{Z}(i,:)$$
(32)

Computing  $\lambda_E$  from Eq. (32) allows for performing the sensitivity analysis of effective ionic conductivity with respect to the design variables by solving the following equation:

$$\frac{d\mathcal{K}_{eff}}{d\hat{\rho}_{i}} = C\left(\mathbb{V}'\frac{\partial\bar{\mathbb{Z}}}{\partial\hat{\rho}_{i}}\right) + \lambda'_{E}\left(\frac{\partial\mathbb{Z}^{*}}{\partial\hat{\rho}_{i}}\mathbb{V}\right) \tag{33}$$

where  $\frac{\partial \overline{\mathbb{Z}}}{\partial \hat{\rho}_i}$  and  $\frac{\partial \mathbb{Z}^*}{\partial \hat{\rho}_i}$  can explicitly be found.

In the thermal module, the p-mean temperature of the domain, which is a differentiable alternative for the maximum temperature (Yang and Chen 1996; Pejman et al. 2019), is considered as the constraint function. We can formulate the p-mean temperature as



$$||T||_{p} = \left(\frac{1}{|\Omega|} \int_{\Omega} (\mathbb{NT})^{p} d\Omega\right)^{1/p} \tag{34}$$

where  $\mid \Omega \mid$  is the volume of the domain. Taking the derivative of Eq. (34) with respect to the projected density yields

$$\frac{d\|T\|_{p}}{d\hat{\rho}_{i}} = \left(\frac{\partial\|T\|_{p}}{\partial\mathbb{T}}\right)'\frac{\partial\mathbb{T}}{\partial\hat{\rho}_{i}} + \frac{\partial\|T\|_{p}}{\partial\hat{\rho}_{i}}$$
(35)

where  $\partial ||T||_p/\partial \mathbb{T}$  can explicitly be found, and  $\partial ||T||_p/\partial \hat{\rho}_i$  is zero. The only unknown in Eq. (35) is temperature sensitivity  $\partial \mathbb{T}/\partial \hat{\rho}_i$ .

Using the adjoint sensitivity analysis method, we annihilate  $\partial \mathbb{T}/\partial \hat{\rho}_i$  from Eq. (35). To do so, we write

$$\frac{d\|T\|_{p}}{d\hat{\rho}_{i}} = \left(\frac{\partial\|T\|_{p}}{\partial\mathbb{T}}\right)' \frac{\partial\mathbb{T}}{\partial\hat{\rho}_{i}} + \lambda'_{T} \left(-\mathbb{K}_{T} \frac{\partial\mathbb{T}}{\partial\hat{\rho}_{i}} +_{T} \mathbb{F}_{pseudo}^{i} \Theta\right)$$
(36)

where  $\lambda_T$  is the arbitrary adjoint variable. Note that the last term in Eq. (36) is zero coming from rearranging the pseudo-problems ( $\mathbb{K}_T \frac{\partial \mathbb{T}}{\partial \alpha_i} = {}_T \mathbb{F}^i_{pseudo}$ ). And the pseudo-

problems are obtained by differentiating the primal problem Eq. (12) with respect to  $\hat{\rho}_i$ . Note that the pseudoforce is  ${}_T\mathbb{F}^i_{pseudo} = -\frac{\partial \mathbb{K}_T}{\partial \hat{\rho}_i}\mathbb{T} + \frac{\partial \mathbb{F}_T}{\partial \hat{\rho}_i}$ .

To determine the adjoint response  $\lambda_T$ , we need to first rearrange the terms in Eq. (36) as follows:

$$\frac{d\|T\|_{p}}{d\hat{\rho}_{i}} = \left( \left( \frac{\partial \|T\|_{p}}{\partial \mathbb{T}} \right)' - {}_{T}^{'} \mathbb{K}_{T} \right) \left( \frac{\partial \mathbb{T}}{\partial \hat{\rho}_{i}} \right) + {}_{T}^{'} \left( -\frac{\partial \mathbb{K}_{T}}{\partial \hat{\rho}_{i}} \mathbb{T} + \frac{\partial \mathbb{F}_{T}}{\partial \hat{\rho}_{i}} \right). \tag{37}$$

We select the adjoint response  $\lambda_T$  in Eq. (37) arbitrarily such that it makes the coefficient of  $\partial \mathbb{T}/\partial \hat{\rho}_i$  zero:

$$\mathbb{K}_{TT}^{'} = \frac{\partial \|T\|_{p}}{\partial \mathbb{T}}.$$
(38)

Hence, by solving Eq. (38),  $\lambda_T$  can be obtained. Consequently, the gradient of  $||T||_p$  with respect to  $\hat{\rho}_i$  is given by

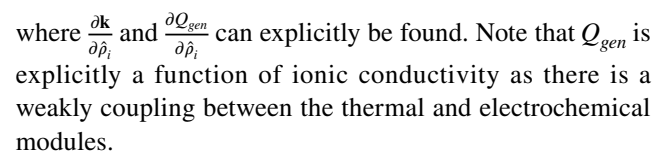
$$\frac{d\|T\|_p}{d\hat{\rho}_i} = T \left( -\frac{\partial \mathbb{K}_T}{\partial \hat{\rho}_i} \mathbb{T} + \frac{\partial \mathbb{F}_T}{\partial \hat{\rho}_i} \right)$$
 (39)

where  $\partial \mathbb{K}_T/\partial \hat{\rho}_i$  and  $\partial \mathbb{F}_T/\partial \hat{\rho}_i$  can be obtained by assembling the element quantity  $\partial \mathbf{K}_T^e/\partial \hat{\rho}_i$  and  $\partial \mathbf{F}_T^e/\partial \hat{\rho}_i$ , respectively.

$$\frac{\partial \mathbf{K}_{T}^{e}}{\partial \hat{\rho}_{i}} = \int_{\Omega} \mathbf{B}_{T}^{e'} \frac{\partial \mathbf{k}}{\partial \hat{\rho}_{i}} \mathbf{B}_{T}^{e'} d\Omega \tag{40}$$

and

$$\frac{\partial \mathbf{F}_{T}^{e}}{\partial \hat{\rho}_{i}} = \int_{\hat{\Omega}} \mathbf{N}_{T}^{e'} \frac{\partial Q_{gen}}{\partial \hat{\rho}_{i}} d\Omega \tag{41}$$



The optimization problem is solved using a fully parallelized implementation of the method of moving asymptotes (MMA) (Svanberg 1987; Aage and Lazarov 2013). Moreover, we take advantage of PETSc (Balay et al. 2021) and MPI to distribute the computational memory and workload over several processors and reduce the computational cost. Note that the accuracy of the derived sensitivity analysis against the finite difference method is confirmed in Appendix D.

# 4 Numerical examples

Two sets of optimization problems are solved to examine the capability of the proposed methodology for designing structural battery electrolyte microstructure. In the first example, the microstructural design of SBE is optimized under the assumption of bulk conditions (*i.e.*, carbon fibers are not considered in the design space). In the second example, the same problem is solved; however, the carbon fibers are explicitly introduced in the design space. Note that in all examples solved in this section, the domain is discretized by  $(128 \times 128 \times 128)$  3-dimensional 8-node hexahedral elements for all analysis modules.

### 4.1 Problem set 1: bulk conditions

The schematic of the problem is shown in Fig. 5. A cubic SBE with a unit length is considered, and it is assumed to be made of a bi-continuous polymer network proposed in Ihrner et al. (2017) with the material properties summarized in Table 1. The pink circles located at the center of the top and beneath surfaces in Fig. 5 indicate the locations where current connectors will attach to the SBE. Note that we do not explicitly consider the current connectors in the problem setup. The radius of these two circles is considered to be a quarter of unit length. In terms of the boundary conditions, a voltage difference of 2.8 V is applied to the SBE. And as mentioned earlier, the current flow is assumed to be in the +Y direction. SBE is considered to be under uniaxial load in the Z direction with the intensity of 10 N. The top and beneath surfaces are assumed to have a convection heat transfer with the ambient environment, and the rest of the surfaces are assumed to be insulated (see Fig. 5). The simulation parameters are summarized in Table 1.

The optimization problem is to optimize the design of bicontinuous SBE, which minimizes compliance and maximizes the effective ionic conductivity. As mentioned earlier, the bicontinuous SBE is composed of two phases: solid and



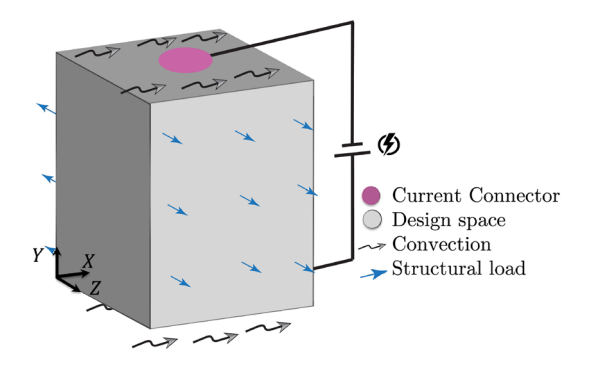


Fig. 5 Schematic of the problem setup for Problem 1

**Table 1** Material properties and simulation parameters

Maximum ionic conductivity of SBE, $\sigma_{max} (S m^{-1})$	1.9(10 <sup>-2</sup> )	Ihrner et al. (2017); Pejman et al. (2021)
Maximum thermal conductivity of SBE, $k_{max}$ $(W m^{-1} K^{-1})$	1	Svensson (2020)
Maximum elastic modulus of SBE, $E_{max}$ ( <i>GPa</i> )	0.5	Ihrner et al. (2017);Pejman et al. (2021)
Poisson's ratio of SBE, <i>v</i>	0.3	Pejman et al. (2021)
Convection coefficient, $h$ $(W m^{-2} K^{-1})$	18	
Ambient temperature, $T_{amb}$ (° $C$ )	25	

compliant. The optimization problem is subjected to a constraint of considering equal volumes for these two phases (i.e., 0.5 volume fraction for each phase). The optimization problem is also subjected to a maximum p-mean temperature constraint of 45 °C. Based on the previous studies in Peiman et al. (2021), p in the p-mean is considered to be 10. The p-mean temperature converges to the maximum temperature when p approaches infinity. However, small values of p can be problematic. Choosing a small value for p may not enable  $||T||_p$  to capture reliably the trend in  $T_{max}$ . Moreover, using large values for p can also be problematic. Since the Gauss–Dunavant quadrature (Dunavant 1985) is used to calculate the integration of p-mean temperature, the larger values of p need more quadrature points which results in a high computational cost. The penalization power p is assumed to be 3. We have implemented the continuation approach to increase the sharpness factor  $\beta$  of Heaviside projection in Eq. (18) gradually from 0.1 to 10 during the optimization process. The threshold value in the Heaviside projection (c.f., Eq. (18)) is considered to be 0.5.  $r_{min}$  in Eq. (19) is assumed to be 0.015. The maximum number of design cycles is assumed to be 100. About 11 million degrees of freedom are considered for this problem to obtain a smooth solution.

NNC method with 9 evenly spaced points on the Utopia line is considered. Ionic conductivity and compliance are considered as  $\theta_1$  and  $\theta_2$  in Eq. (16), respectively. Note that instead of maximizing ionic conductivity, we minimize the negative of ionic conductivity.

The optimization result is shown in Fig. 6. The number of design cycles required for convergence of each one of the NNC's 9 evenly spaced points in this example was less than 60. Furthermore, due to the non-convex nature of the gradient-based topology optimization method used in this study, the optimization problem is solved from 10 distinct initial guesses to increase the chance of reaching a better local optimized solution. However, obviously, the algorithm cannot guarantee to reach global optimal points. The Pareto front curve is generated as shown in Fig. 6a. Points A and C in Fig. 6a indicate the optimized designs for the electrochemical purpose (i.e., maximum ionic conductivity) and structural purpose (i.e., maximum stiffness), respectively. The design is gradually converging from the optimized electrochemical design (Point A in Fig. 6a) to optimized structural design (Point C in Fig. 6a) as we increase the *j* value in Eq. (17). To better represent the details of the optimized solutions, the ISO-view and cross-sectional views of Points A, B, and C are shown in Fig. 6b-d, respectively.

The results reveal that the optimizer considers the compliant phase (indicated by pink color in Fig. 6b) for top and beneath surfaces to facilitate the ion transfer. This leads to a higher effective ionic conductivity based on Eq. (7). In terms of minimizing compliance, as the structural performance gets dominant in the Pareto front curve, the optimizer considers the solid phase (indicated by green color in Fig. 6c) for the surfaces where the structural load is applied. Note that Point B on the Pareto front curve represents a trade-off between the electrochemical and structural demands from SBE (*i.e.*, showing both high ionic conductivity and high stiffness.).

As mentioned earlier, a weakly coupling between thermal and electrochemical physics is considered for the computation of the Ohmic heat generation rate. Thus, satisfying the temperature constraint is more concerning for all the points between A to B on the Pareto front curve that has larger ionic conductivity (leading to a higher Ohmic heat generation rate). It is also worth mentioning that the top and bottom surfaces have convection heat transfer with the ambient environment, thus, their temperature is lower than the insulated surfaces (*i.e.*, side surfaces). As a result, the optimizer can



46 Page 10 of 17 R. Pejman, A. R. Najafi

Fig. 6 a Pareto front curve obtained by using the NNC method for optimization problem 1. The ISO-view and cross-sectional views for Points b A, c B, and d C. Note that Point A is the optimized solution for having maximum ionic conductivity, and Point C is the optimized solution for having maximum stiffness

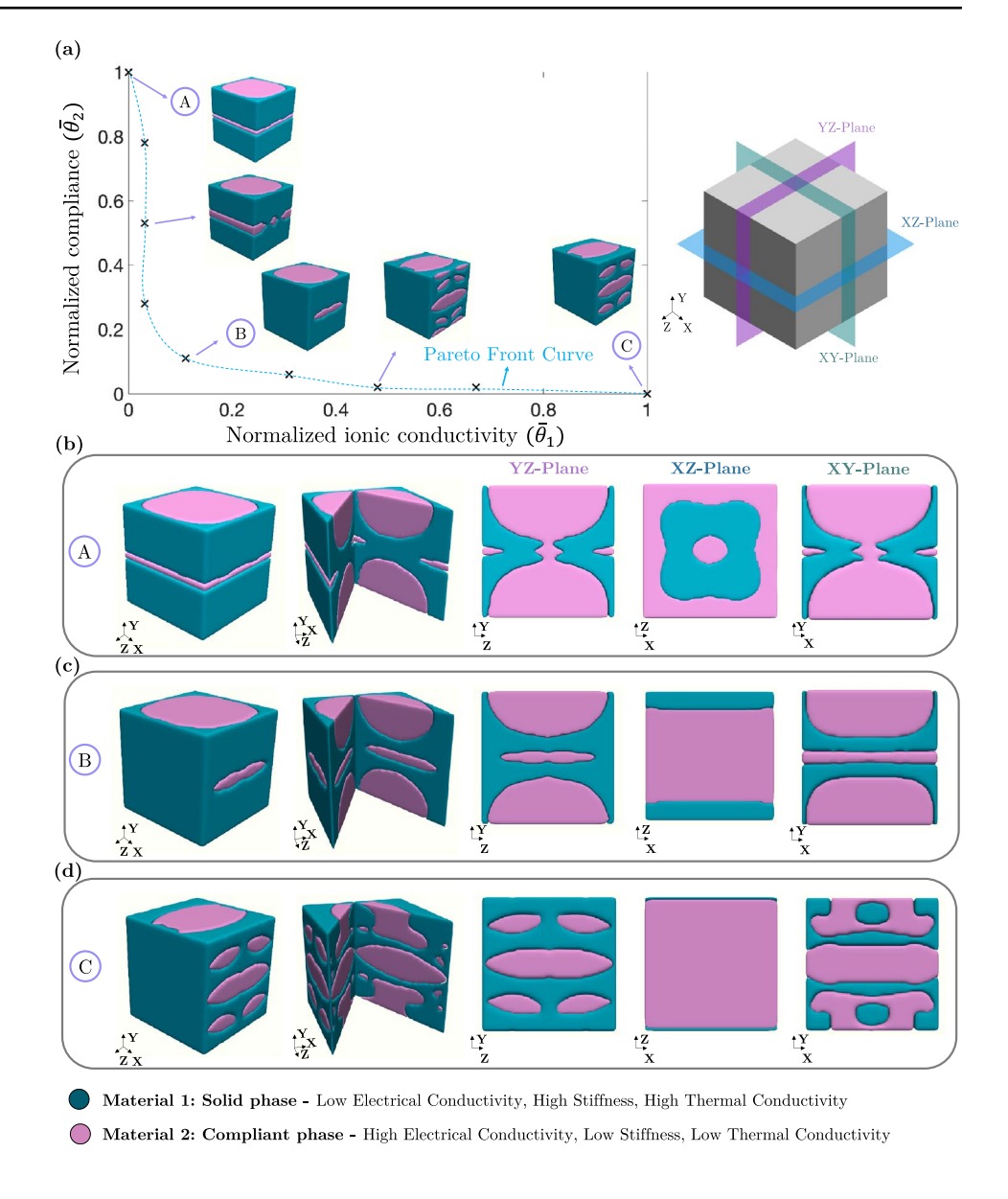
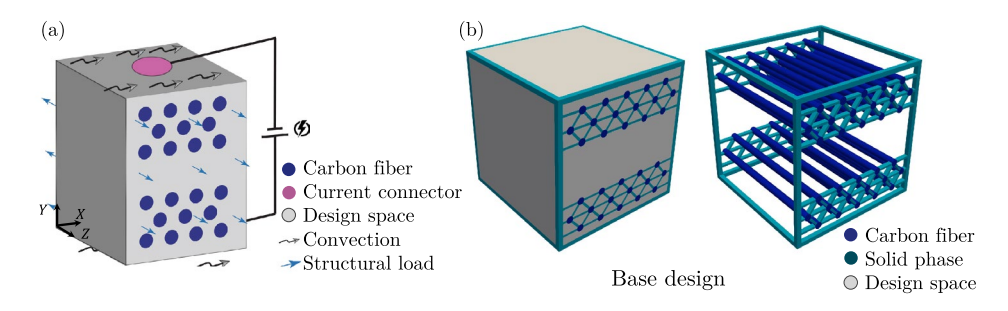


**Fig. 7** a Schematic of the problem setup for Problem 2, **b** the base frame design considered for avoiding structurally unsupported fibers in the optimized design



use more of the compliant phase that has a lower thermal conductivity on top and beneath surfaces as temperature rise is not a major concern over there.

### 4.2 Problem set 2: explicit carbon fibers

### 4.2.1 Tensile load

As mentioned earlier, the expectation is to see a different



Table 2 Material properties of carbon fiber

Ionic conductivity of carbon fiber, $\sigma_{cf}$ ( $S \ cm^{-1}$ )	714	Kjell et al. (2011); Pej man et al. (2021)
Thermal conductivity of carbon fiber, $k_{cf}$ ( $W m^{-1} K^{-1}$ )	35.1	Fredi et al. (2018)
Elastic modulus of carbon fiber, $E_{cf}$ ( $GPa$ )	294	Fredi et al. (2018)
Poisson's ratio of carbon fiber, $v_{cf}$	0.45	Pejman et al. (2021)

optimized microstructure from that in the bulk condition when introducing reinforcement fibers. Thus, in this section, we solve the same optimization problem as the problem set 1, however, we consider the carbon fibers in the problem setup as shown in Fig. 7a. All the material properties and simulation parameters are the same as in Problem 1. Carbon fibers are assumed to be made of T800 and it is treated as passive elements during the optimization process. The material properties of carbon fiber are summarized in Table 2.

To make sure that the carbon fibers will be structurally supported in the optimized solution, we consider a base frame design as shown in Fig. 7b. The green frame indicates passive elements that are considered to be made of the solid phase of the bicontinuous SBE.

The NNC Pareto front curve associated with this optimization problem is shown in Fig. 8a. Point A in Fig. 8a is the first anchor point in the NNC method that has  $\bar{\theta}_1 = 0$  and  $\bar{\theta}_2 = 1$ . It is indeed the optimized design for having maximum ionic conductivity. The cross-sectional views of its design are represented in Fig. 8b. Point C in Fig. 8a is the other anchor point of the NNC method that indicates the optimized design obtained from the minimization of the compliance. Figure 8d shows the cross-sectional views of Point C design. And finally, Point B in Fig. 8a is one the middle Pareto front points that its detailed design is represented in Fig. 8c. As expected, comparing the solutions obtained in Problem sets 1 and 2 (Figs. 6 and 8) confirms that considering carbon fibers explicitly in the design space alters the obtained optimized solutions.

### 4.2.2 Shear load

Uniaxial tensile and shear loads are often considered as practical load-bearing requirements for matrix/electrolytes in multifunctional composites (Shirshova et al. 2013; Lee et al. 2019). Thus, we also examine the proposed design framework for the same optimization problem but under shear load, as shown in Fig. 9.

The results related to this optimization problem are demonstrated in Fig. 10. Figure 10a shows the optimized design obtained by solving the single-objective problem of maximizing ionic conductivity. Note that this design is exactly similar to the design obtained in Problem set 2 under tensile load (Fig. 8b). This behavior is completely expected as structural performance is not playing any role in this part of the optimization problem (*i.e.*, the single-objective problem of maximizing ionic conductivity).

Figure 10b demonstrates the optimized design by solving the NNC multi-objective optimization problem with  $\frac{N-j}{N-1} = \frac{j-1}{N-1} = 0.5$ . And Fig. 10c represents the optimized design obtained by solving the single-objective problem of minimizing compliance. As opposed to the tensile load case, the optimizer makes the top and bottom surfaces completely solid phase for better structural performance.

# 5 Contributions, limitations, and future directions

The major contributions of this study are as follows:

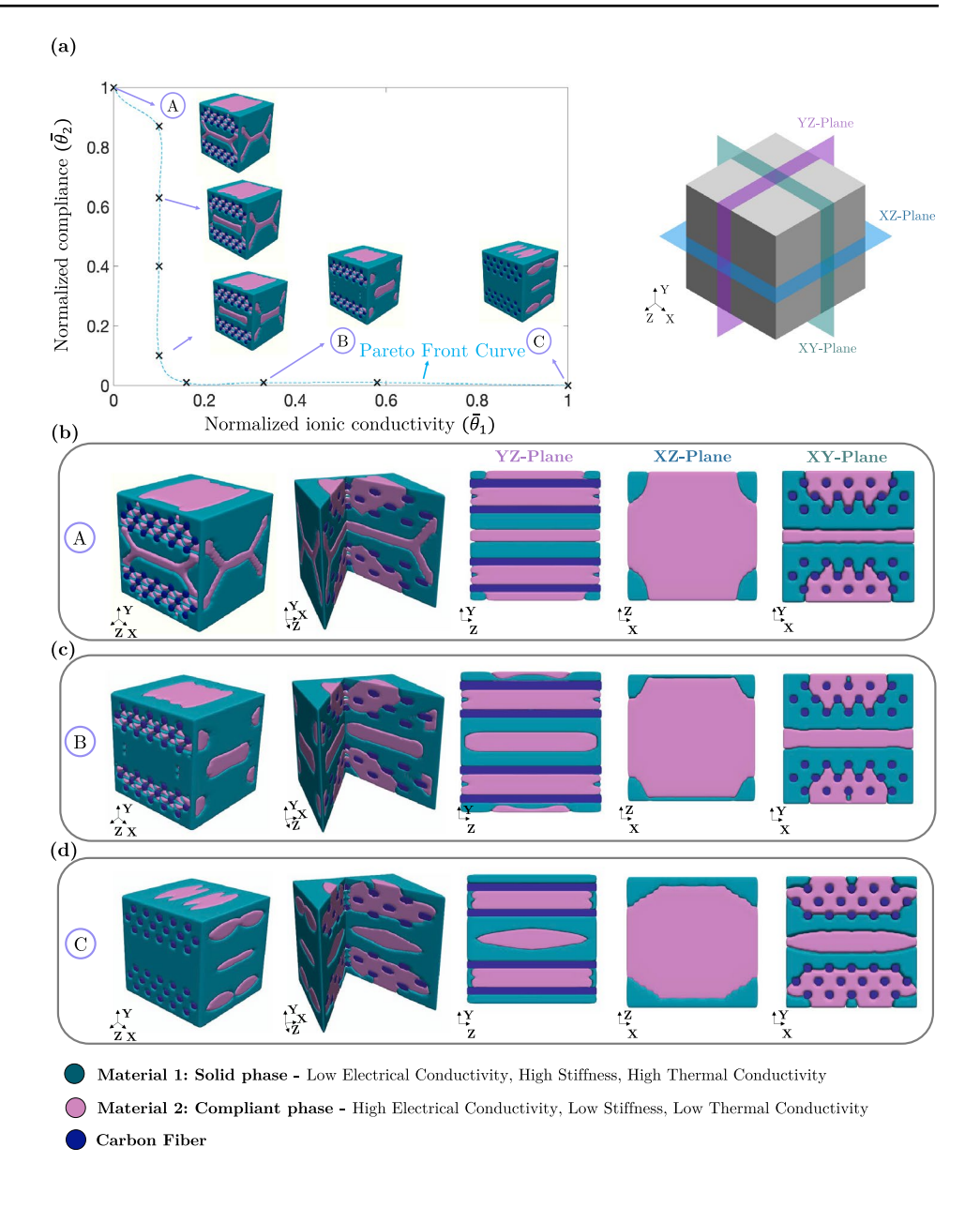
- To the best of our knowledge, this study is the first to develop a systematic multi-objective topology optimization framework for the design of SBE microstructure by simultaneously considering three physics (electrochemical, structural, and thermal). In this multiphysics problem, the thermal module is weakly-coupled to the electrochemical module since the amount of generated heat in the SBE is computed using the Ohmic heat generation equation.
- To the best of our knowledge, this study is the first to develop a sensitivity analysis for the ResNet approach to be used as the electrochemical module in the proposed design approach.
- This study addresses the issue mentioned in Asp and Greenhalgh (2015) (i.e., designing SBE microstructure by considering carbon fibers in the design space).

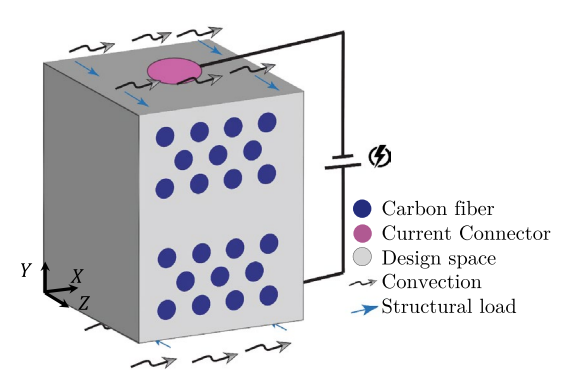
One of the current limitations of the proposed approach is that the two-way coupling between the electrochemical/structural/thermal modules is not considered. Hence, in future work, the method can be extended to consider the two-way coupling between the electrochemical/structural/thermal modules. For instance, damage in the microstructure impacts the effective ionic conductivity and stiffness. And the temperature rise in the microstructure results in thermal strains.



46 Page 12 of 17 R. Pejman, A. R. Najafi

Fig. 8 a Pareto front curve associated with the optimization problem 2 under uniaxial tensile load. The ISO-view and cross-sectional views for Points b A, c B, and d C. Note that Point A is the optimized solution for having maximum ionic conductivity, and Point C is the optimized solution for havingmaximum stiffness





 $\begin{tabular}{ll} Fig. 9 & Schematic of the problem setup for Problem set 2 under shear load \\ \end{tabular}$ 

6 Conclusion

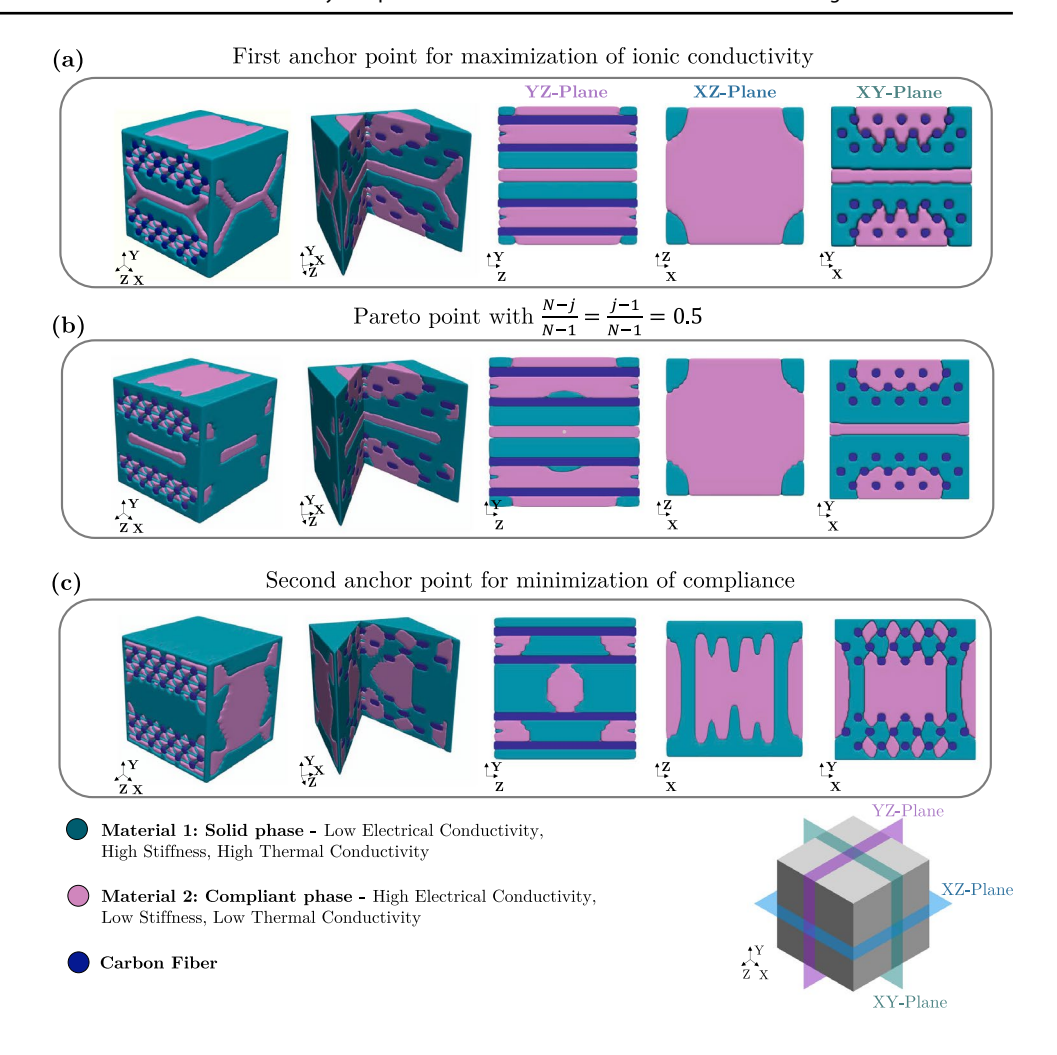
structure incorporated in the SBC.

The motivation of this study is to address one of the challenges in the development of structural battery composites (SBC), which is associated with the existence of a conflict in the structural, electrical, and thermal demands for its electrolyte. To this end, a multi-objective multiphysics

Furthermore, in this study, the results reveal that considering carbon fibers explicitly in the design space leads to a different optimized microstructure than the bulk condition. As a future study, the shape optimization method can be used to optimize the location and shape of the carbon fiber



Fig. 10 Optimized designs of Problem set 2 under shear load obtained by solving a maximization of ionic conductivity, **b** NNC multi-objective optimization problem with  $\frac{N-j}{N-1} = \frac{j-1}{N-1} = 0.5$ , and **c** minimization of compliance



gradient-based topology optimization methodology is presented to tailor the design of structural battery electrolytes (SBE). The SBE in a structural battery composite needs to both transfer the structural load and work as a lithium-ion battery electrolyte. SBE is expected to have high stiffness and ionic conductivity and it should not generate substantial heat. The need to fulfill these disparate features generates intrinsically conflicting physical property demands. One possible strategy that is considered in this study is to optimize a bi-continuous architecture of two distinct phases for the electrolyte, each addressing different physical demands. Thus, the optimization approach is to solve a multi-objective problem of maximizing effective ionic conductivity and minimizing compliance of structural battery electrolytes. The problem is subjected to constraints on volume fraction and maximum allowable temperature to prevent it from overheating. The most important findings of the study have been listed in the following:

 Utilizing the normalized-normal-constraint (NNC) approach, we generate a Pareto-front curve for the design of SBE.

- With reference to the verification studies performed in Appendix C and Appendix D, we conclude that the analysis and sensitivity analysis modules developed in this study showed acceptable accuracy.
- The obtained results reveal that as hypothesized in Asp and Greenhalgh (2015), considering carbon fibers explicitly in the design space alters the obtained optimized solutions for SBE.
- Our results also confirm that having better control of the design of SBE can have a significant effect on the performance improvement of energy-harvesting battery composites.
- Using the proposed multi-objective multiphysics design approach in this study allows for designing an SBE microstructure that has high ionic conductivity and high stiffness while working at a safe operating temperature.
- The proposed design approach considers a weakly coupling between the electrochemical and thermal modules.
   However, the method can be extended to consider the two-way coupling between the electrochemical/structural/thermal modules.



46 Page 14 of 17 R. Pejman, A. R. Najafi

# Appendix A: Finite element discretization of structural module

For the structural module explained in Sect. 2.2, the approximation of the displacement field in each element is given by

$$U_e^h(\mathbf{X}) = \sum_{i=1}^{n_S^e} N_i(\mathbf{X}) U_i = \mathbf{N}_S^e(\mathbf{X}) \mathbf{U}^e$$
(A1)

where

$$\mathbf{N}_{S}^{e} = \begin{bmatrix} N_{1} & 0 & 0 & N_{2} & 0 & 0 & \dots & N_{n_{S}^{e}} & 0 & 0 \\ 0 & N_{1} & 0 & 0 & N_{2} & 0 & 0 & 0 & N_{n_{S}^{e}} & 0 \\ 0 & 0 & N_{1} & 0 & 0 & N_{2} & 0 & 0 & 0 & N_{n_{S}^{e}} \end{bmatrix}$$

$$= [N_{1} \ N_{2} \ \dots \ N_{n_{S}^{e}}] \odot \mathbf{I}$$
(A2)

$$\mathbf{U}^{e} = [U_{1}^{x} \ U_{1}^{y} \ U_{1}^{z} \ U_{2}^{x} \ U_{2}^{y} \ U_{2}^{z} \ \dots \ U_{n_{s}^{e}}^{x} \ U_{n_{s}^{e}}^{y} \ U_{n_{s}^{e}}^{z}]'$$
(A3)

 $\odot$  is the Kronecker product, **I** is a 3 × 3 identity matrix, **X** is the spatial coordinates,  $n_S^e$  is the number of finite element shape functions,  $N_i(\mathbf{X})$  is the finite element shape functions, and  $U_i$  is the nodal displacement. The notation (.)' denotes transpose.

As mentioned in Sect. 2.2, implementation of the FEM leads to Eq. (8), in which  $\mathbf{K}_{S}^{e}$  is a function of  $\mathbf{B}_{S}^{e}$  and  $\mathbb{C}$  defined by

$$\mathbf{B}_{S}^{e} = \begin{bmatrix} \frac{\partial N_{1}}{\partial x} & 0 & 0 & \dots & \frac{\partial N_{n_{S}^{e}}}{\partial x} & 0 & 0 \\ 0 & \frac{\partial N_{1}}{\partial y} & 0 & \dots & 0 & \frac{\partial N_{n_{S}^{e}}}{\partial y} & 0 \\ 0 & 0 & \frac{\partial N_{1}}{\partial z} & \dots & 0 & 0 & \frac{\partial N_{n_{S}^{e}}}{\partial z} \\ \frac{\partial N_{1}}{\partial x} & \frac{\partial N_{1}}{\partial y} & 0 & \dots & \frac{\partial N_{n_{S}^{e}}}{\partial x} & \frac{\partial N_{n_{S}^{e}}}{\partial y} & 0 \\ 0 & \frac{\partial N_{1}}{\partial y} & \frac{\partial N_{1}}{\partial z} & \dots & 0 & \frac{\partial N_{n_{S}^{e}}}{\partial x} & \frac{\partial N_{n_{S}^{e}}}{\partial z} \\ \frac{\partial N_{1}}{\partial x} & 0 & \frac{\partial N_{1}}{\partial z} & \dots & 0 & \frac{\partial N_{n_{S}^{e}}}{\partial x} & 0 \\ \frac{\partial N_{1}}{\partial x} & 0 & \frac{\partial N_{1}}{\partial z} & \dots & \frac{\partial N_{n_{S}^{e}}}{\partial x} & 0 & \frac{\partial N_{n_{S}^{e}}}{\partial z} \\ \end{bmatrix}$$

$$(A4)$$

and

$$\mathbb{C} = 2\mu \mathbb{P}_{Sym} + \lambda \mathbf{I} \otimes \mathbf{I} \tag{A5}$$

where  $\otimes$  is dyadic product,  $\lambda = \frac{vE}{(1+v)(1-2v)}$  is Lamé moduli,  $\mu = \frac{E}{2(1+v)}$  is the shear modulus, E is the modulus of elasticity, v is the Poisson ratio, and  $\mathbb{P}_{Sym}$  is the 4-tensor symmetric projection, i.e.,  $\mathbb{P}_{Sym}[\mathbf{A}] = (\mathbf{A} + \mathbf{A}')/2$ .

# Appendix B: Finite element discretization of thermal module

The temperature field approximation in each element can be written as



$$T_e^h(\mathbf{X}) = \sum_{i=1}^{n_T^e} N_i(\mathbf{X}) T_i = \mathbf{N}_T^e(\mathbf{X}) \mathbf{T}^e$$
 (B6)

where

$$\mathbf{N}_{T}^{e} = [N_{1} \ N_{2} \ \dots \ N_{n_{T}^{e}}] \tag{B7}$$

$$\mathbf{T}^{e} = [T_{1} \ T_{2} \ \dots \ T_{n_{x}^{e}}]'$$
 (B8)

 $n_T^e$  is the number of degrees of freedoms (dof) in each element and  $T_i$  is the nodal temperature.

As mentioned in Sect. 2.3, implementing FEM results leads to Eq. (12), in which  $\mathbf{K}_T^e$  is a function of  $\mathbf{B}_T^e$  defined by

$$\mathbf{B}_{T}^{e} = \begin{bmatrix} \frac{\partial N_{1}}{\partial x} & \frac{\partial N_{2}}{\partial x} & \dots & \frac{\partial \hat{N}_{n_{T}^{e}}}{\partial x} \\ \frac{\partial N_{1}}{\partial y} & \frac{\partial N_{2}}{\partial y} & \dots & \frac{\partial \hat{N}_{n_{T}^{e}}}{\partial y} \\ \frac{\partial N_{1}}{\partial z} & \frac{\partial N_{2}}{\partial z} & \dots & \frac{\partial \hat{N}_{n_{T}^{e}}}{\partial z} \end{bmatrix}$$
(B9)

# **Appendix C: Verification of analysis modules**

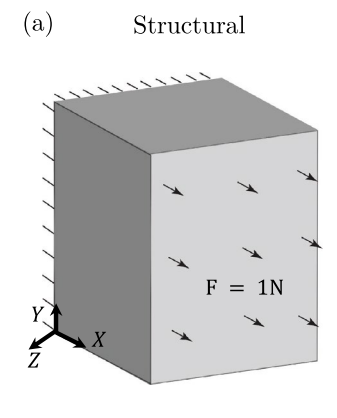
The structural and thermal modules developed in this study are verified against ANSYS structural and ANSYS FLU-ENT, respectively. The problem setup for this verification study is presented in Fig. 11. Thermal conductivity and modulus of elasticity of the sample are assumed to be  $1 \ Wm^{-1}K^{-1}$  and  $0.5 \ GPa$ , respectively. The boundary conditions are presented in Fig. 12. For the structural problem, the sample is assumed to be under a tensile load in the X-direction. And in the thermal problem, the sample is assumed to have convection heat transfer on front and back surfaces, and the rest of the surfaces are considered to be insulated. Constant heat generation of  $24 \ W/m^3$  is considered for this problem.

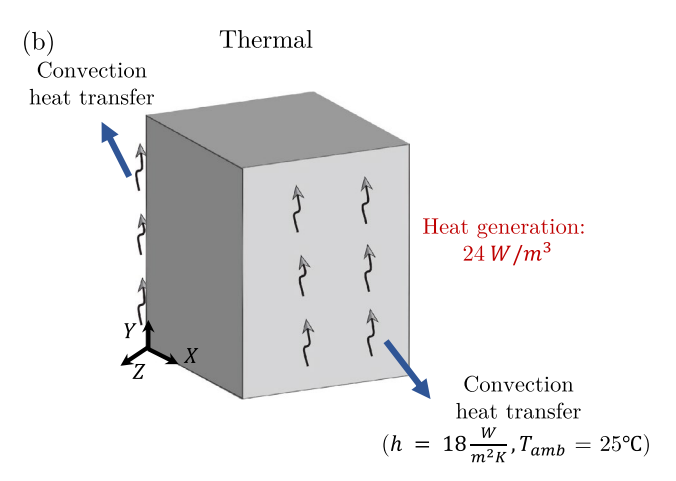
Figure 12 compares temperature and displacement distributions obtained from ANSYS and the analysis code in this study. The results are quite close to each other as the L2-norm difference between the in-house code and ANSYS for T,  $U_x$ ,  $U_y$ , and  $U_z$  are  $0.02^{\circ}C$ ,  $0.001 \, \mu m$ ,  $0.0004 \, \mu m$ , and  $0.0004 \, \mu m$ , respectively. Hence, we can conclude that the structural and thermal analysis modules developed in this study have acceptable accuracy. Note that the accuracy of the electrochemical module is checked and confirmed against the test cases provided in Rhazaoui et al. (2013).

# Appendix D: Verification of sensitivity analysis

We perform a verification study of the analytic adjoint sensitivity analysis developed in this study by comparing it with the central finite difference method. The error between the adjoint and finite difference sensitivity analysis is given by

**Fig. 11** Problem setup for verification study for **a** structural and **b** thermal modules





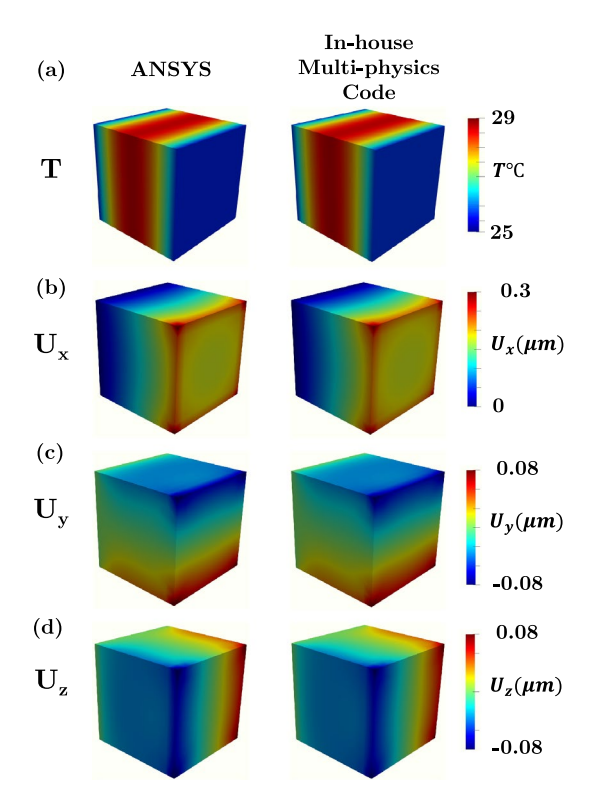


Fig. 12 Comparison between ANSYS and the multiphysics code for  ${\bf a}$  temperature,  ${\bf b}$  x-component of displacement,  ${\bf c}$  y-component of displacement, and  ${\bf d}$  z-component of displacement distributions

$$\epsilon = \left| \frac{\left(\frac{d\theta}{dd_i}\right)^{Adj} - \left(\frac{d\theta}{dd_i}\right)^{FD}}{\left(\frac{d\theta}{dd_i}\right)^{Adj}} \right| \tag{D10}$$

where Adj and FD indicate the adjoint method and finite difference approach, respectively. The error is plotted in Fig. 13 for a sequence of perturbations from  $\Delta d_i = 10^{-2} - 10^{-7}$  for all three physics of electrochemical, thermal, and structural. Note that  $\theta$  in Eq. (D10) indicates ionic conductivity,

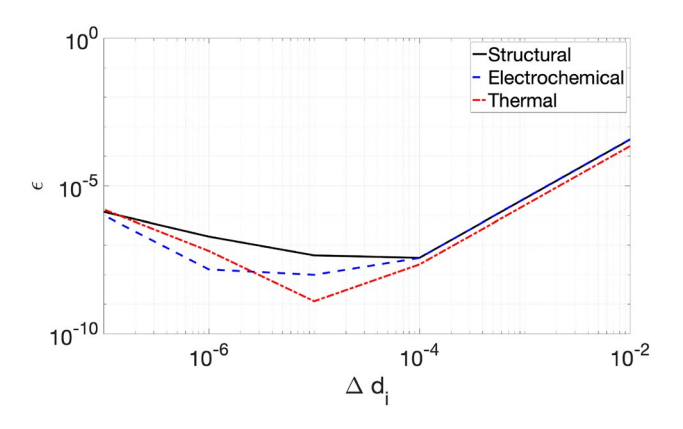


Fig. 13 The relative error,  $\epsilon$ , between the adjoint sensitivity analysis and approximated central finite difference sensitivity versus the magnitude of the perturbation in the design parameter,  $\Delta d_i$ . The amount of error is quite small and we can conclude that the sensitivity analysis is correctly derived and implemented in this study

compliance, and p-mean temperature for electrochemical, structural, and thermal physics, respectively. The relative error has a small value, which indicates that the sensitivity analysis is correctly derived and implemented.

**Acknowledgements** The work is supported by the NSF CAREER Award CMMI-2143422. This work is also supported by Drexel University Career Development Award. The authors acknowledge the high-performance computing resources and support at Drexel University. The authors would also like to thank Nolan Black for insightful discussions related to this work.

### **Declarations**

Conflict of interest The authors declare no competing interests.

**Replication of results** We provided comprehensive implementation details, and as a result, we are confident that the design methodology is reproducible. For this reason, we have decided not to publish the code. If the information provided in the paper is not sufficient, the readers are welcome to contact the authors for further explanations.



46 Page 16 of 17 R. Pejman, A. R. Najafi

### References

- Aage N, Lazarov BS (2013) Parallel framework for topology optimization using the method of moving asymptotes. Struct Multidisc Optim 47(4):493–505
- Aage N, Andreassen E, Lazarov BS (2015) Topology optimization using petsc: an easy-to-use, fully parallel, open source topology optimization framework. Struct Multidisc Optim 51(3):565–572
- Asp LE (2013) Multifunctional composite materials for energy storage in structural load paths. Plast Rubber Compos 42(4):144-149
- Asp LE, Greenhalgh ES (2014) Structural power composites. Compos Sci Technol 101:41–61
- Asp LE, Greenhalgh ES (2015) Multifunctional structural battery and supercapacitor composites. Multifunctionality of Polymer Composites-Challenges and New Solutions, pp 619–661
- Balay S, Abhyankar S, Adams MF, Benson S, Brown J, Brune P,
  Buschelman K, Constantinescu E, Dalcin L, Dener A, Eijkhout V, Gropp WD, Hapla V, Isaac T, Jolivet P, Karpeev D, Kaushik D, Knepley MG, Kong F, Kruger S, May DA, McInnes LC,
  Mills RT, Mitchell L, Munson T, Roman JE, Rupp K, Sanan P, Sarich J, Smith BF, Zampini S, Zhang H, Zhang J
  (2021) PETSc/TAO users manual. Technical Report ANL-21/39 Revision 3.16, Argonne National Laboratory
- Beringer I, Walter M, Snyder J, Wetzel E (2018) Multifunctional structural polymer electrolytes via interpenetrating truss structures. Multifunct Mater 1(1):015005
- Borrvall T, Petersson J (2003) Topology optimization of fluids in stokes flow. Int J Numer Methods Fluids 41(1):77–107
- Bruns TE, Tortorelli DA (2001) Topology optimization of non-linear elastic structures and compliant mechanisms. Comput Methods Appl Mech Eng 190(26–27):3443–3459
- Carlstedt D, Asp LE (2019) Thermal and diffusion induced stresses in a structural battery under galvanostatic cycling. Compos Sci Technol 179:69–78
- Carlstedt D, Asp LE (2020) Performance analysis framework for structural battery composites in electric vehicles. Compos Part B Eng 186:107822
- Choi H, Berson A, Pharoah J, Beale S (2011) Effective transport properties of the porous electrodes in solid oxide fuel cells. Proc Inst Mech Eng Part A J Power Energy 225(2):183–197
- Cuong-Le T, Minh HL, Khatir S, Wahab MA, Tran MT, Mirjalili S (2021) A novel version of cuckoo search algorithm for solving optimization problems. Exp Syst Appl 186:115669
- Dede EM (2009) Multiphysics topology optimization of heat transfer and fluid flow systems. In: Proceedings of the COMSOL Users Conference
- Dunavant D (1985) High degree efficient symmetrical Gaussian quadrature rules for the triangle. Int J Numer Methods Eng 21(6):1129–1148
- Ekstedt S, Wysocki M, Asp L (2010) Structural batteries made from fibre reinforced composites. Plast Rubber Compos 39(3-5):148-150
- Fredi G, Jeschke S, Boulaoued A, Wallenstein J, Rashidi M, Liu F, Harnden R, Zenkert D, Hagberg J, Lindbergh G et al (2018) Graphitic microstructure and performance of carbon fibre liion structural battery electrodes. Multifunct Mater 1(1):015003
- Gersborg-Hansen A, Bendsøe MP, Sigmund O (2006) Topology optimization of heat conduction problems using the finite volume method. Struct Multidisc Optim 31(4):251–259
- Guest JK (2009) Imposing maximum length scale in topology optimization. Struct Multidisc Optim 37(5):463–473
- Guest JK, Prévost JH (2006) Optimizing multifunctional materials: design of microstructures for maximized stiffness and fluid permeability. Int J Solids Struct 43(22–23):7028–7047

- Guest JK, Prévost JH, Belytschko T (2004) Achieving minimum length scale in topology optimization using nodal design variables and projection functions. Int J Numer Methods Eng 61(2):238-254
- Holmberg E, Torstenfelt B, Klarbring A (2014) Fatigue constrained topology optimization. Struct Multidisc Optim 50(2):207–219
- Ihrner N, Johannisson W, Sieland F, Zenkert D, Johansson M (2017) Structural lithium ion battery electrolytes via reaction induced phase-separation. J Mater Chem A 5(48):25652–25659
- Johannisson W, Zenkert D, Lindbergh G (2019) Model of a structural battery and its potential for system level mass savings. Multifunct Mater 2(3):035002
- Kambampati S, Jauregui C, Museth K, Kim HA (2020) Large-scale level set topology optimization for elasticity and heat conduction. Struct Multidisc Optim 61(1):19–38
- Kambampati S, Gray JS, Kim HA (2021) Level set topology optimization of load carrying battery packs. Int J Heat Mass Transf 177:121570
- Khatir S, Wahab MA (2019) Fast simulations for solving fracture mechanics inverse problems using pod-rbf xiga and jaya algorithm. Eng Fract Mechan 205:285–300
- Khatir S, Wahab MA, Boutchicha D, Khatir T (2019) Structural health monitoring using modal strain energy damage indicator coupled with teaching-learning-based optimization algorithm and isogoemetric analysis. J Sound Vib 448:230–246
- Khatir S, Boutchicha D, Le Thanh C, Tran-Ngoc H, Nguyen T, Abdel-Wahab M (2020) Improved ann technique combined with jaya algorithm for crack identification in plates using xiga and experimental analysis. Theor Appl Fract Mech 107:102554
- Khatir S, Tiachacht S, Le Thanh C, Ghandourah E, Mirjalili S, Wahab MA (2021) An improved artificial neural network using arithmetic optimization algorithm for damage assessment in fgm composite plates. Compos Struct 273:114287
- Kjell MH, Jacques E, Zenkert D, Behm M, Lindbergh G (2011) Panbased carbon fiber negative electrodes for structural lithium-ion batteries. J Electrochem Soc 158(12):1455
- Larsen UD, Signund O, Bouwsta S (1997) Design and fabrication of compliant micromechanisms and structures with negative poisson's ratio. J Microelectromech Syst 6(2):99–106
- Le C, Norato J, Bruns T, Ha C, Tortorelli D (2010) Stress-based topology optimization for continua. Struct Multidisc Optim 41(4):605-620
- Lee C, Greenhalgh ES, Shaffer MS, Panesar A (2019) Optimized microstructures for multifunctional structural electrolytes. Multifunct Mater 2(4):045001
- Liu P, Sherman E, Jacobsen A (2009) Design and fabrication of multifunctional structural batteries. J Power Sour 189(1):646–650
- Maskery I, Aremu A, Parry L, Wildman R, Tuck C, Ashcroft I (2018) Effective design and simulation of surface-based lattice structures featuring volume fraction and cell type grading. Mater Design 155:220–232
- Matsumori T, Kondoh T, Kawamoto A, Nomura T (2013) Topology optimization for fluid-thermal interaction problems under constant input power. Struct Multidisc Optim 47(4):571–581
- Messac A, Ismail-Yahaya A, Mattson CA (2003) The normalized normal constraint method for generating the pareto frontier. Struct Multidisc Optim 25(2):86–98
- Mu D, Liu Z-S, Huang C, Djilali N (2007) Prediction of the effective diffusion coefficient in random porous media using the finite element method. J Porous Mater 14(1):49–54
- Onishi J, Kametani Y, Hasegawa Y, Shikazono N (2019) Topology optimization of electrolyte-electrode interfaces of solid oxide fuel cells based on the adjoint method. J Electrochem Soc 166(13):876
- Panesar A, Abdi M, Hickman D, Ashcroft I (2018) Strategies for functionally graded lattice structures derived using topology optimisation for additive manufacturing. Addit Manuf 19:81–94



- Pejman R, Aboubakr SH, Martin WH, Devi U, Tan MHY, Patrick JF, Najafi AR (2019) Gradient-based hybrid topology/shape optimization of bioinspired microvascular composites. Int J Heat Mass Transf 144:118606
- Pejman R, Kumbur EC, Najafi AR (2021) Multi-physics design optimization of structural battery. Multifunct Mater 4(2):024001
- Pejman R, Sigmund O, Najafi AR (2021) Topology optimization of microvascular composites for active-cooling applications using a geometrical reduced-order model. Struct Multidisc Optim 2021:1–21
- Pejman R, Gorman J, Najafi AR (2022) Multi-physics design of a new battery packaging for electric vehicles utilizing multifunctional composites. Compos Part B Eng 2022:109810
- Rhazaoui K, Cai Q, Adjiman C, Brandon N (2013) Towards the 3d modeling of the effective conductivity of solid oxide fuel cell electrodes: I. model development. Chem Eng Sci 99:161–170
- Rhazaoui K, Cai Q, Adjiman C, Brandon N (2014) Towards the 3d modeling of the effective conductivity of solid oxide fuel cell electrodes-ii. computational parameters. Chem Eng Sci 116:781-792
- Rhazaoui K, Cai Q, Kishimoto M, Tariq F, Somalu M, Adjiman C, Brandon N (2015) Towards the 3d modelling of the effective conductivity of solid oxide fuel cell electrodes-validation against experimental measurements and prediction of electrochemical performance. Electrochim Acta 168:139–147
- Rozvany G (2001) Topology optimization in structural mechanics. Struct Multidisc Optim 21(2):89
- Shirshova N, Bismarck A, Carreyette S, Fontana QP, Greenhalgh ES, Jacobsson P, Johansson P, Marczewski MJ, Kalinka G, Kucernak AR et al (2013) Structural supercapacitor electrolytes based on bicontinuous ionic liquid-epoxy resin systems. J Mater Chem A 1(48):15300–15309
- Snyder JF, Carter RH, Wetzel ED (2007) Electrochemical and mechanical behavior in mechanically robust solid polymer electrolytes for use in multifunctional structural batteries. Chem Mater 19(15):3793–3801
- Snyder J, Baechle D, Wetzel E, Xu K (2008) Multifunctional structural composite batteries for us army applications. Technical report, Army Research Lab Aberdeen Proving Ground Md
- Svanberg K (1987) The method of moving asymptotes-a new method for structural optimization. Int J Numer Methods Eng 24(2):359–373

- Svensson N (2020) Thermo-mechanical modelling of structural battery composites
- Tran-Ngoc H, Khatir S, Ho-Khac H, De Roeck G, Bui-Tien T, Wahab MA (2021) Efficient artificial neural networks based on a hybrid metaheuristic optimization algorithm for damage detection in laminated composite structures. Compos Struct 262:113339
- Wang F, Lazarov BS, Sigmund O (2011) On projection methods, convergence and robust formulations in topology optimization. Struct Multidisc Optim 43(6):767–784
- Wetzel ED (2004) Reducing weight: multifunctional composites integrate power, communications and structure. AMPTIAC Q 8(4):91–95
- Willgert M, Kjell MH, Jacques E, Behm M, Lindbergh G, Johansson M (2011) Photoinduced free radical polymerization of thermoset lithium battery electrolytes. Europ Polymer J 47(12):2372–2378
- Wong E, Baechle D, Xu K, Carter R, Snyder J, Wetzel E (2007) Design and processing of structural composite batteries. Technical report, Army Research Lab Aberdeen Proving Ground MD
- Xu K (2004) Nonaqueous liquid electrolytes for lithium-based rechargeable batteries. Chem Rev 104(10):4303–4418
- Yaji K, Yamasaki S, Tsushima S, Suzuki T, Fujita K (2018) Topology optimization for the design of flow fields in a redox flow battery. Struct Multidisc Optim 57(2):535–546
- Yang R, Chen C (1996) Stress-based topology optimization. Struct Optim 12(2–3):98–105
- Zhao X, Zhou M, Sigmund O, Andreasen CS (2018) A "poor man's approach" to topology optimization of cooling channels based on a Darcy flow model. Int J Heat Mass Transf 116:1108–1123
- Zhu X, Zhao C, Wang X, Zhou Y, Hu P, Ma ZD (2019) Temperatureconstrained topology optimization of thermo-mechanical coupled problems. Eng Optim 51:1

**Publisher's Note** Springer Nature remains neutral with regard to jurisdictional claims in published maps and institutional affiliations.

Springer Nature or its licensor (e.g. a society or other partner) holds exclusive rights to this article under a publishing agreement with the author(s) or other rightsholder(s); author self-archiving of the accepted manuscript version of this article is solely governed by the terms of such publishing agreement and applicable law.

